Journal of Materials Chemistry A

ROYAL SOCIETY OF CHEMISTRY

PAPER

View Article Online
View Journal | View Issue



Cite this: J. Mater. Chem. A, 2020, 8, 10252

# Thermodynamic and dynamic dual regulation $Bi_2O_2CO_3/Bi_5O_7I$ enabling high-flux photogenerated charge migration for enhanced visible-light-driven photocatalysis†

Yan Guo,[a] Jun Nan,[a] Yongpeng Xu,[a] Fuyi Cui,[b] Wenxin Shi *[ab] and Yongfa Zhu*[c]

Received 5th March 2020
Accepted 24th April 2020

DOI: 10.1039/d0ta02588g

rsc.li/materials-a

Herein, the essence of high-flux photogenerated charge migration for $Bi_2O_2CO_3/Bi_5O_7I$ heterojunction photocatalysts is revealed from both thermodynamic and dynamic perspectives. The appropriate energy band offset provides the thermodynamic conditions of photogenerated electrons and holes migration in opposite directions, which is derived from the lower valence and conduction band positions of $Bi_5O_7I$ than $Bi_2O_2CO_3$. Meanwhile, the dynamic conditions are provided by the interface electric field generated *via* the work function difference between $Bi_5O_7I$ and $Bi_2O_2CO_3$, which affords a driving force for the above-mentioned reverse migration of photogenerated electrons and holes. Moreover, the Bi–O chemical bond on the interface creates a charge transport bridge between $Bi_5O_7I$ and $Bi_2O_2CO_3$. By benefiting from the dual regulation of thermodynamics and dynamics and the charge transport bridge, the photocatalytic activity of the $Bi_2O_2CO_3/Bi_5O_7I$ heterojunction photocatalyst has significantly increased at least 23 times under visible light irradiation. This finding could also be applied to other fields to tune the optimal charge transport performance of heterojunctions.



## Introduction

The separation and migration of photogenerated carriers are key factors that determine photocatalytic performance.[1–3] A semiconductor heterojunction is an effective way to promote the separation of photogenerated charges.[4] Type II junctions have been widely investigated as an effective strategy for photocatalysis applications due to their interface interaction, allowing directional electron transport.[5,6] However, the ambiguity of the effect of the interface interaction on photoinduced charge transfer severely limits the further design and development of heterojunction photocatalysts. Most of the work reported in the literature on heterojunction photocatalysts elaborates on the migration direction of photogenerated charges at the interface, from the perspective of band position matching. There have also been several reports that the interfacial electric field improves the separation effect of photogenerated electron–hole pairs, but still lack in-depth research to quantify the built-in electric field.[7–9] In other words, the adjustment of photogenerated charge by a heterojunction has explained the possibility of this phenomenon from the perspective of thermodynamics. However, the influence of the driving force on the speed of photogenerated charge transfer still needs to be considered further; that is, the dynamic conditions are not used as a measure of the heterojunction material. It is well known that thermodynamics and dynamics are complementary and are two indispensable branches for studying reactions. Therefore, there is an urgent need to achieve the dual regulation of heterojunction photocatalysts from the perspectives of thermodynamics and dynamics.

More importantly, the charge transfer performance of heterojunctions is limited by the migration of random charge accumulation and depletion layer formation of different materials. However, a large number of migration channels for interfacial charges are able to effectively reduce this limitation.[10] The 2D–2D heterojunction connected by a van der Waals force is widely reported in the literature.[11,12] However, as a van der Waals force is an instantaneous induction of an electric dipole moment, it decreases rapidly with increasing distance leading to a weak interface interaction force. In contrast, an interface formed with chemical bonds creates a much stronger interaction force between the atoms at the contact interface, accompanied by changes in atomic electronic structure.[13,14] Therefore, the interface connected by chemical bonds provides stable migration bridges for continuous charge transfer, and effectively avoids the random accumulation of charges.[15,16]

[a]State Key Laboratory of Urban Water Resource and Environment, School of Environment, Harbin Institute of Technology, Harbin 150090, China. E-mail: swx@hit.edu.cn

[b]School of Environment and Ecology, Chongqing University, Chongqing, 400044, China

[c]Department of Chemistry, Tsinghua University, Beijing, 100084, China. E-mail: zhuyf@tsinghua.edu.cn

† Electronic supplementary information (ESI) available. See DOI: 10.1039/d0ta02588g

Zhang's group found that the photocatalytic degradation of contaminants can act as a carbon source lead to one-unit-cell $Bi_2O_2CO_3$ layers which grow *in situ* from the surface of a $Bi_2O_4$ photocatalyst during the progress of photodegradation, and finally form a heterojunction $Bi_2O_4/Bi_2O_2CO_3$.[17] Li's group constructed $Bi_2Ti_2O_7/\gamma$-$Bi_2O_3$ by *in situ* fabrication, where $\gamma$-$Bi_2O_3$ acts as a support and tertbutyl titanite as the titanium source. The co-sharing of the Bi–O structure helps to fabricate a tightly connected interface.[18] Hou's group reported the synthesis of mesoporous heterostructures $In_2O_3$–$x$/$In_2S_3$ through the *in situ* oxidation of $In_2S_3$ atomic layers *via* an oxygen plasma-induced strategy.[19] Moreover, they also proposed an *in situ* phase-induced etching chemical strategy to prepare the $Ta_3N_5$@NaTaON heterojunction with a strong interfacial Ta–O–N bonding connection.[10] Without exception, these heterojunctions are formed by producing another substance *in situ* on one substance. Inspired by these reports, we used *in situ* conversion of $Bi_5O_7I$ to fabricate $Bi_5O_7I/Bi_2O_2CO_3$ for the following reasons: (1) *in situ* conversion is conducive to the building of an interface contacted with Bi–O bonds between $Bi_5O_7I$ and $Bi_2O_2CO_3$, which is expected to provide a smooth charge separation pathway; (2) preparation of the structure can easily be controlled by adjusting the reaction conditions of *in situ* conversion; (3) due to the Bi source control, the interface between $Bi_5O_7I$ and $Bi_2O_2CO_3$ is effectively regulated, while forming a nanostructure; (4) carbonate is derived from the oxidation of organic matter during the a hydrothermal reaction, which is beneficial in controlling the thickness and scale of $Bi_2O_2CO_3$.

Guided by this line of thinking, and based on our previous research on bismuth oxyiodide, $Bi_5O_7I$ (BOI; which has the greatest photocatalytic potential in bismuth oxyiodide)[20] and $Bi_2O_2CO_3$ (BOC; which has regular layered structure) were selected to form an interface. In this work, we prepared a BOC/BOI type II heterojunction photocatalyst by means of the *in situ* conversion *via* a simple one-pot hydrothermal method. The Bi–O chemical bond at the heterojunction interface provides a path for the continuous transmission of photogenerated charges, thereby realizing high-flux photogeneration charge transfer. More importantly, from the perspective of thermodynamics, the possibility of the direction of photogenerated charge transfer is explained by the theory of interfacial band offset. Also, from the perspective of dynamics, the interfacial electric field provides the driving force for high-speed migration of photogenerated charges. Thus, the nature of $Bi_2O_2CO_3/Bi_5O_7I$, which achieved efficient separation with minimal recombination, was revealed. As direct evidence of the success of this approach, the photocatalytic activity of the $Bi_2O_2CO_3/Bi_5O_7I$ heterojunction significantly increased by at least 23 times under visible light.

# Experimental

### Sample preparation

Different ratios of $Bi_2O_2CO_3/Bi_5O_7I$ (BOC/BOI) heterojunctions were prepared by adjusting the ratio of glycerol as a carbon source. First, BOI was formed at room temperature, then glycerol was oxidized to carbonate in a solvothermal reaction, and BOI was converted *in situ* to BOC.

For the $Bi_2O_2CO_3/Bi_5O_7I$ heterojunctions, 0.486 g (1 mmol) of $Bi(NO_3)_3\cdot 5H_2O$ was dissolved in 40, 25 or 5 ml of deionized water, then 10, 25 or 45 ml of glycerol was added with vigorous stirring for 30 min, followed by addition of 5 ml deionized water dissolved with 1 mmol KI and 0.24 g KOH. The resulting solution was transferred to a 100 ml polytetrafluoroethylene-lined autoclave and heated at 160 °C for 6 h. The final product was washed six times with deionized water and absolute ethanol and dried at 60 °C. Samples were denoted as: BOC/BOI-1, BOC/BOI-2 and BOC/BOI-3 (where 1, 2, 3 respectively represent the ratio of glycerol in the solvent is 0.2, 0.5, 0.9).

For the synthesis of $Bi_2O_2CO_3$, 25 ml of glycerol and 25 ml of water were used as the solvent, no KI was added, and the rest of the procedure was as described above.

For the synthesis of $Bi_5O_7I$, 50 ml of water was used as a solvent, and the rest of the procedure was as described above.

### Sample characterization

Powder X-ray diffraction (XRD) patterns of the samples were obtained on a Bruker D8 X-ray diffractometer with Cu K$\alpha$ radiation ($\lambda$ = 0.15418 nm). The morphologies of the samples were analyzed by scanning electron microscopy (SEM) using a ZEISS Sigma 500 instrument, transmission electron microscopy (TEM) on a JEOL JEM-1400 TEM at an accelerating voltage of 100 kV and high-resolution transmission electron microscopy (HRTEM) on a Tecnai F20 instrument operating at an accelerating voltage of 200 kV. X-ray photoelectron spectroscopy (XPS) was performed using a Thermo ESCALAB 250 instrument with Al K$\alpha$ X-ray ($h\nu$ = 1486.6 eV) radiation. Ultraviolet-visible (UV-vis) diffuse reflection spectra (DRS) were obtained on a spectrophotometer (Shimadzu, UV2550) with $BaSO_4$ as reference. Brunauer, Emmett and Teller (BET) surface area measurements were recorded on an ASAP2020 instrument. Steady-state photoluminescence (PL) spectra were detected using a Perkline LS55 fluorescence spectrophotometer with $\lambda_{ex}$ = 250 nm. Surface photovoltage (SPV) spectra were recorded using home-built apparatus, equipped with a lock-in amplifier (SR830, USA) synchronized with a light chopper (SR540, USA). For transient-state surface photovoltage (TS-SPV) responses of the samples, the samples were excited by a radiation pulse of 355 nm with 10 ns width from the second harmonic of a neodymium-doped yttrium aluminum garnet (Nd:YAG) laser (Lab-130-10H, Newport, Co.) and the signals were amplified with a pre-amplifier and registered with a 1 GHz digital phosphor oscilloscope (DPO 4104B, Tektronix).

Photoelectrochemical measurements were performed on a CHI-660 E (China) electrochemical workstation with a standard three-electrode cell, including counter electrode (Pt wire), reference electrode (saturated calomel electrode) and working electrodes (as-prepared samples covered indium tin oxide [ITO] glass). $Na_2SO_4$ (0.1 M) was used as the electrolyte solution. For the working electrodes, a sample (2 mg) was dispersed in Nafion solution (naphthol : ethanol = 1 : 9) to obtain a slurry. Then the slurry was coated onto the ITO glass and dried in an oven overnight. Electrochemical impedance spectroscopy spectra were recorded under an AC perturbation signal of 10 mV over the frequency range from 100 kHz to 1 Hz.

### Photocatalytic performance evaluation

Photocatalytic activity was estimated by measuring the degradation of bisphenol A (BPA), 4-chlorophenol (4-CP), 2,4-dichlorophenol (2,4-DCP) and phenol. In a static photocatalytic system, 50 mg samples were dispersed in 100 ml of BPA (4-CP, 2,4-DCP and phenol) solution with 10 ppm under $\lambda \geq 420$ nm irradiation. Before the light irradiation, the mixture was stirred for 30 min to reach the adsorption equilibrium in the dark. The temperature of the reactor was maintained at 20 °C by continuous circulating water. The continuous flow reaction was conducted in a fixed bed reactor with 50 mg of BOC/BOI-2 photocatalyst loaded in the groove (40 mm × 20 mm × 2 mm), with the two opposite sides serving as the import and export. A 300 W xenon lamp equipped with a $\lambda \geq 420$ nm cut-off filter was placed above the reactor as the light source. The 10 mg $L^{-1}$ BPA solution was fed by a peristaltic pump with a constant flow rate of 1 ml $min^{-1}$. At given irradiation time intervals, about 2 ml of the solution was taken out to analyze the residual contaminant concentration. The concentration was detected using a high-performance liquid chromatography (HPLC) system (Waters Baseline 810) with a Waters 486 tunable UV absorbance detector and a Supelco LC-18-DB column (250 mm × 4.6 mm). Total organic carbon (TOC) analyzer (Multi N/C 2100s) was employed for mineralization degree analysis of pollutants.

### Theoretical calculations

All theoretical calculations were performed through the generalized gradient approximation (GGA) within the Perdew–Burke–Emzerhof (PBE) exchange-correlation functional implemented in the CASTEP code. The ultrasoft pseudopotential in the Vanderbilt form was used for description of ion–electron interactions. The plane-wave function was set with a cut-off energy of 420 eV. Geometry optimizations were performed before single point energy calculation with a self-consistent convergence accuracy of $1 \times 10^{-5}$ eV per atom. The convergence criterion for the maximal force between atoms is 0.03 eV $Å^{-1}$. The maximum displacement is $1 \times 10^{-3}$ Å, and the stress is less than 0.05 GPa.

## Results and discussion

### Dual regulation of thermodynamics and dynamics for BOC/BOI heterojunction with charge transfer bridges

First-principle calculations were used to examine the thermodynamic and dynamic conditions for the BOC/BOI heterojunction. Density functional theory (DFT) calculations show the inconsistent width of the forbidden band between BOC and BOI (Fig. S1†), which means a band exists offset at the interface.[21] The relative positions of the energy bands of the two semiconductors determine the migration direction of the photogenerated electrons and holes at the interface; that is, the thermodynamic conditions. To elucidate the direction of the interface charge migration determined by the band offset, the energy band alignment structure was extracted by experimental characterization (Fig. S2a–c†). The conduction band (CB) offset ($\Delta E_c$) produced at the bottom of the CB was +0.12 eV, and the valence band (VB) offset ($\Delta E_v$) generated at the bottom of the VB was +0.37 eV (Fig. 1a and S2d; for the specific calculation see ESI†).[22] The calculation of the energy band step directly indicates that the positions of the VB and the CB of BOC are higher than those of BOI. Therefore, the thermodynamic conditions provided by the energy band offset enable holes to migrate from BOI to BOC, and the reverse for electrons.

According to the work function difference, when BOC and BOI are in contact, an electron would flow from the BOI with low work function (2.4 eV) to the BOC with high work function (2.6 eV) until the Fermi energy level was balanced (Fig. S3†).[18,23] A depletion layer and an accumulation layer of electrons are respectively formed at BOI and BOC meanwhile, and an energy barrier ($qV_{barrier}$) of about 0.2 eV is generated, thereby forming a band bend and an interfacial electric field (IEF) directed from the BOI to the BOC (Fig. 1b).[24–26] It is well known that the electric field influences the migration of interface charges. The electric field force accelerates the forward electric field movement of positive charges and the reverse electric field movement of negative charges. Fortunately, the direction of the IEF at the BOC/BOI interface is the same (opposite) to the direction of movement of the photogenerated holes (electrons), determined by the above thermodynamic conditions. In fact, for BOC/BOI, it can be predicted that the dynamic result must accelerate the direction of photogenerated charge as determined by thermodynamics. This is because the direction of the IEF must be from a material with a small work function to a large work function. According to the above DFT calculation, it is known that the work function of BOI is smaller than that of BOC. The thermodynamic conditions provided by the energy band position allow photogenerated holes to be transferred from the BOI to BOC. It cannot be ignored that the IEF directed from BOI to BOC

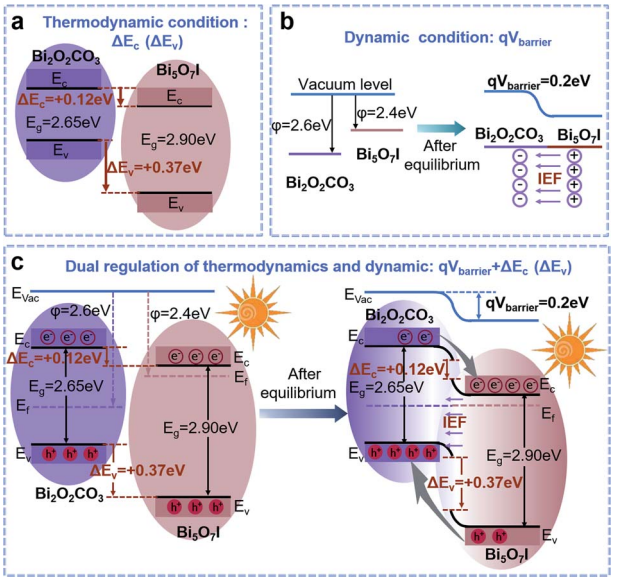


Fig. 1 Schematic thermodynamic conditions: $\Delta E_c$ ($\Delta E_v$) (a); dynamic condition: $qV_{barrier}$ (b); dual regulation of thermodynamics and dynamic for BOC/BOI heterojunction (c).

 

provides a driving force for the transfer motion of photogenerated charges to achieve a dynamic acceleration process. The photogenerated holes of BOI arrive at the VB of the BOC, and then migrate to the surface of the BOC. The direction of motion of the photogenerated electrons is the opposite. In this process, thanks to the kinetic acceleration process offered by IEF, the photogenerated electron–hole pairs are effectively separated. Eventually, photogenerated holes and electrons arriving at the surfaces of BOC and BOI participate in oxidation and reduction reactions, respectively. At this point, the thermodynamic conditions indicate the possibility of the directional migration of photogenerated charges at the interface, and the dynamic condition demonstrates this movement is an accelerated process. As a result, BOC/BOI achieves both thermodynamic and dynamic regulation; $qV_{barrier} + \Delta E_v(\Delta E_c)$ (Fig. 1c).

The interface effect plays an important role during the photogenerated charge transfer process.[27–30] Because the interface without tight connection does not support to the charge transmission at the interface. Providing efficient transport pathways has been used to maximize the efficiency of photogenerated charge utilization.[19,31] Compared with pure material, the partial projected density of states (PDOS) have a higher coincidence for heterojunction (Fig. S4†), which shows their electronic states are highly hybrid and increases the chance of charge transfer at the interface.[32] To reveal the presence of Bi–O chemical bonds between the BOC and BOI, the static charge changes of the interface atoms were first analyzed. Compared with pure substances, the Bi static charge at the interface was significantly changed, which indicates that charge transfer occurred after the formation of the heterojunction, resulting in strong Bi–O electron coupling (see Fig. S5 and Table S1† for specific analysis). Moreover, taking the charge density map containing Bi1–O1 as an example (Fig. S6†), the electron density at the interface was strong around the O1 of the BOI, but weak for the Bi1 of the BOC, which confirms close electronic coupling between BOI and BOI. Then, after avoiding the error of the inherent atomic static charge value and expressing the net change in the spatial distribution of the charge, the differential charge density difference also suggests that Bi–O has electron accumulation and depletion at the interface (Fig. S7†). The bond levels further illustrate that the electron coupling originates from the presence of Bi–O bonds at the interface (see Table S2† for the specific analysis). These theoretical results confirm the constructing carrier migration channels of the Bi–O bond is a candidate for a weak recombination effect.

### *In situ* conversion to prepare a BOC/BOI heterojunction

Motivated by these theoretical calculations, we synthesized a BOC/BOI heterojunction *via* a one-pot *in situ* conversion. XRD, FT-IR and XPS were used to demonstrate that the heterojunctions were successfully obtained by *in situ* conversion (see Fig. S8† for specific analysis). Fig. 2a shows the *in situ* conversion process of BOC on BOI by replacement reaction. First, a thick board BOI was produced at room temperature (Fig. S9a and S10a†), then $CO_3^{2-}$ favorably bonded with the surface of BOI under electrostatic forces during the hydrothermal reaction, next the BOI surface began to transform into the BOC piece and eroded into the block itself. Sufficient $CO_3^{2-}$ continued to corrode the surface of the BOI to nanorods, and the BOC became thinner, transforming into two-dimensional (2D) nanosheets in subsequent reactions. Finally, a nano heterojunction BOC/BOI-2 with a large contact area was obtained (Fig. S9c and S10c†). However, too little of the carbon source caused the reaction to stay at step 3, forming a micron-sized heterojunction (Fig. S9b and S10b†), while excessive carbon source resulted in serious agglomeration (Fig. S9d and S10d†). The illustration in Fig. 2b shows the two-phase boundary of BOC/BOI-2 and a large contact area benefiting from the flakes and the small size of the nanorods. Further, the lattice fringes of

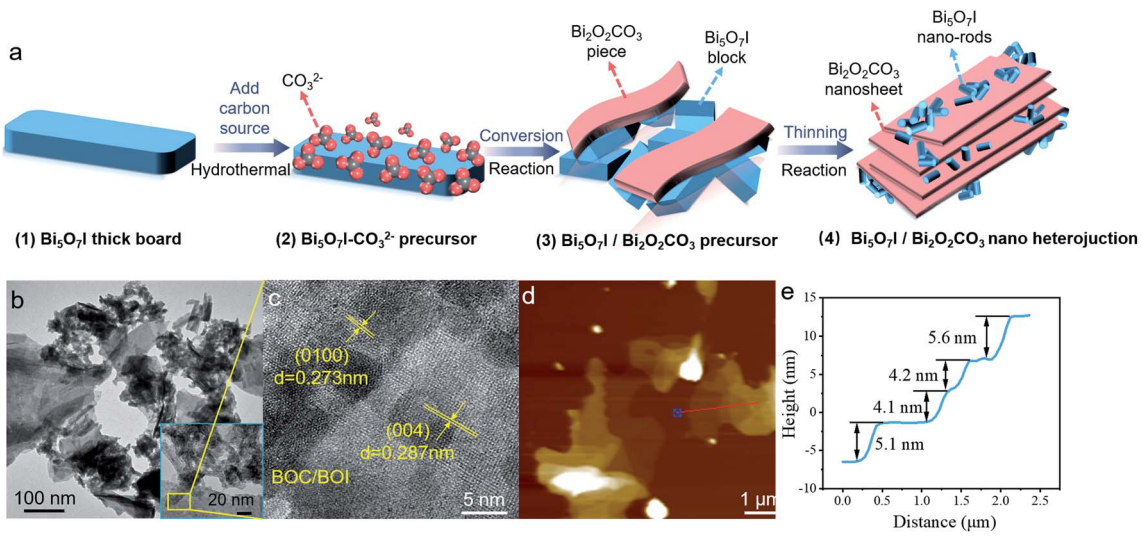


Fig. 2 (a) Schematic illustration of the preparation of BOC/BOI-2; (b) TEM; (c) HRTEM; (d) AFM image; (e) the corresponding height profile of BOC/BOI-2.

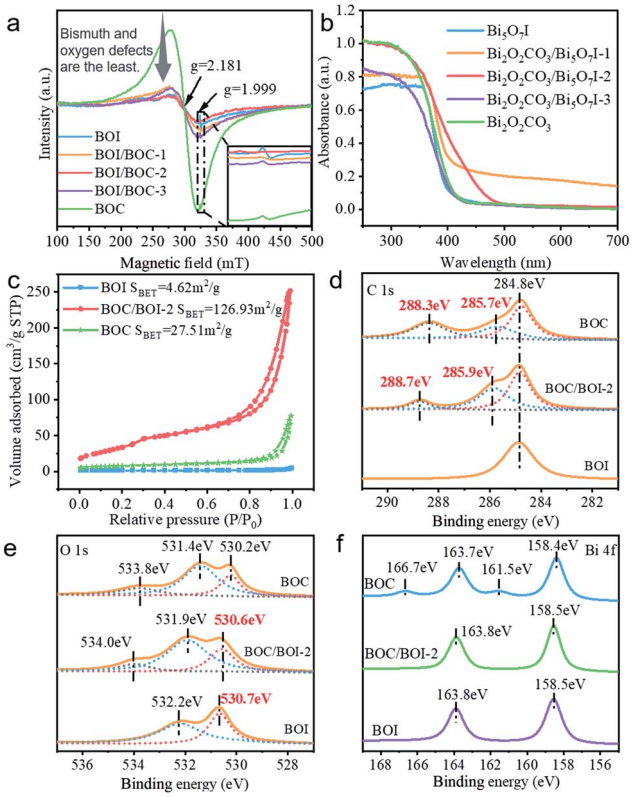


Fig. 3 (a) ESR spectra; (b) UV-vis diffuse reflection spectra; (c) $N_2$ adsorption–desorption isotherms of as-prepared samples. High resolution XPS spectra of (d) C 1s; (e) O 1s; (f) Bi 4f.

0.273 nm and 0.283 nm correspond to the (0,10,0) crystal plane of BOC and (0,0,4) of BOI, respectively (Fig. 2c). Atomic force microscopy (AFM) shows that the thickness of these sheets is ~5 nm (Fig. 2d and e), which directly confirms that BOC is a 2D sheet. Furthermore, electron paramagnetic resonance (EPR) was performed on the prepared samples (Fig. 3a), which is a sensitive and direct technique for monitoring the behavior of material surface defects. The peaks at $g = \sim 2.1$ (ref. 33 and 34) and $g = \sim 2.0$ (ref. 35) represent bismuth defects and oxygen defects, respectively. Interestingly, compared with the other synthetic samples, BOC/BOI-2 has the fewest bismuth defects, and the EPR signal of BOC/BOI-2 oxygen deficiency was barely detected. The fewer defects of BOC/BOI-2, the more regular the lattice, meaning that the local state proportion caused by defects in the lattice is reduced. In contrast, when the degree of delocalization is increased, the degree of commonality is increased.[36,37] The results of energy band broadening, reducing the band gap, and red-shifting the absorbed light were obtained by BOC/BOI-2 (Fig. 3b). Note that the specific surface area of the nano heterojunction BOC/BOI-2 (up to 126.93 $m^2\ g^{-1}$) is significantly larger than that of BOI (4.62 $m^2\ g^{-1}$) and BOC (27.51 $m^2\ g^{-1}$), which provides efficient diffusion and transportation in degradation (Fig. 3c). Moreover, 2D with a high specific surface area helps to form a large contact area at the interface, thereby making it possible for the interface to dominate. Although BOC/BOI heterojunctions can be prepared with different proportions of carbon source dosing, there is an optimal amount of carbon source dosing to give the prepared heterojunction a neat morphology and a larger contact interface. Considering that the morphology affects the transfer of charges on the semiconductor, the large contact interface determines the amount of separated photogenerated charges, meaning that BOC/BOI-2 has more advantages.

The realization of BOC/BOI-2 allows the use of XPS to investigate DFT relating to Bi–O bonds at the interface. Generally, the XPS binding energy is negatively correlated with the surface electron density.[38] The binding energies of 288.3 and 285.7 eV characterizing C=O and C–O in BOC increase to 288.7 and 285.9 eV,[39] which is attributed to the strong interaction between BOC and BOI affecting the electrons of C in $CO_3^{2-}$ (Fig. 3d). The binding energy of 530.7 eV in BOI is ascribed to Bi–O, which is shifted down to 530.6 eV after forming a heterojunction,[40] because the Bi electron of BOC at the interface transfers to the O atom of BOI to form strong Bi–O chemical bonds (Fig. 3e). Meanwhile, the higher binding energies of 166.7 and 161.5 eV appeared in the spectrum of BOC (Fig. 3f), which is also consistent with its strongest Bi defect signal, as shown in Fig. 3a. As mentioned earlier, theoretical calculations show that strong Bi–O chemical bonds tightly connect BOC and BOI to form a strong interaction interface. Experimental characterization confirms that among the BOC/BOI heterojunctions prepared using different carbon source dosing ratios, the interface of BOC/BOI-2 is closest to the result of the theoretical calculations.

## Dual regulation and charge transfer bridges promote photogenerated charge separation

Next, the effect of dual regulation and bridges at the interface on photogenerated charge separation were explored. The charge transfer resistance of the photocatalyst is simulated by using the equivalent circuit R(C(R(QR))) (CR) of Fig. 4a, according to electrochemical impedance spectroscopy (EIS). The analog charge transfer resistance of BOC/BOI-2 (724.9 Ω $cm^{-2}$) is far less than that of the BOI (1032 Ω $cm^{-2}$) and BOC (2913 Ω $cm^{-2}$), showing that the bridges reduce the charge transfer resistance between the BOC and BOI. The BOC/BOI-2 quenches the steady-state PL intensity of BOI and BOC by 76.3% and 67.2%, respectively (Fig. 4b), meaning a decrease in the recombination of photogenerated electron–hole pairs. The excellent separation effect promotes extensive photogenerated charges to reach the surface of the photocatalyst, which is proven by the strongest photocurrent density (Fig. 4c) and SPV signal (Fig. 4d) of BOC/BOI-2. Subsequently, the charge recombination efficiencies of BOC/BOI-2 were quantitatively measured with open circuit potential (OCP) transients. Fig. 4e compares the attenuation curve of OCP after turning off the light among as-prepared samples without externally applied bias. The average recombination constant is estimated by normalizing the OCP signal and fitting the data to a first-order dynamic model (eqn (1)):[41,42]

$$\frac{E_t - E_{ph}}{E_{da} - E_{ph}} = 1 - \exp^{-kt} \quad (1)$$

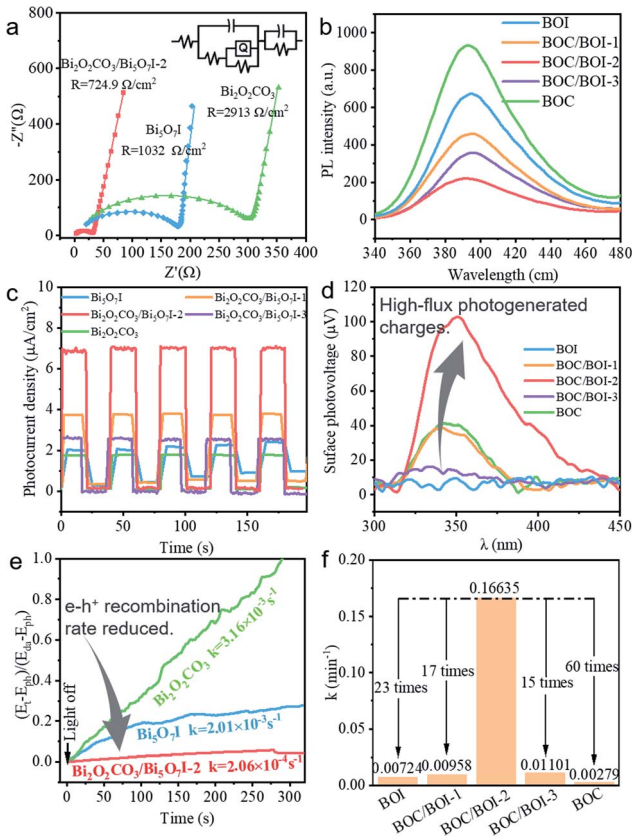


Fig. 4 (a) Electrochemical impedance spectroscopy (EIS); (b) photoluminescence spectra (PL) at 250 nm excitation wavelength; (c) photocurrent under $\lambda \geq 420$ nm; (d) surface photovoltage irradiation; (e) normalized open-circuit potential (OCP) attenuation curves after turning off the $\lambda \geq 420$ nm irradiation for samples prepared; (f) the apparent reaction rate constants for BPA under visible light ($\lambda \geq 420$ nm) irradiation.

where $E_t$ is the OCP over time, $E_{da}$ is the static OCP value in the dark, $E_{ph}$ is the steady OCP value under visible light illumination and $k$ is the pseudo first-order recombination rate constant. The OCP decay dynamics reflect the charge recombination and show how the heterojunction alters recombination. The fitted $k$ of BOC/BOI-2 ($2.06 \times 10^{-4}$ $s^{-1}$) is reduced by 90% and 96% compared with BOI ($2.01 \times 10^{-3}$ $s^{-1}$) and BOC ($3.16 \times 10^{-3}$ $s^{-1}$), respectively. The OCP decay is significantly retarded for BOC/BOI-2 due to lots of channels at the interface avoiding random accumulation and the recombination of photogenerated charges. These results strongly suggest that constructing dual regulation and generous bridges at the interface is a promising approach to improve photogenerated charge transfer by inhibiting recombination.

The photoactivity is highly correlated with the charge separation efficiency, and the ameliorative photogenerated charge transfer endowed BOC/BOI-2 with visible photoactivity for degradation. The apparent rate constants of BOC/BOI-2 with outstanding activity are 23-, 17-, 15- and 60-times those of BOI, BOC/BOI-1, BOC/BOI-3 and BOC, respectively (Fig. 4f and S11†). Moreover, BOC/BOI-2 shows remarkable photodegradation of BPA activity under visible light compared with other reported photocatalysts, as presented in Table S5.† The results in Fig. S12† demonstrate the universality of BOC/BOI-2 for photodegradation of organic pollutants. Next, the TOC removal results show that BOC/BOI-2 has acceptable salinity for different pollutants due to its good oxidizing ability (Fig. S13†). In addition, the excellent recycling performance of the BOC/BOI-2 heterojunction is shown in Fig. S14.† Moreover, the EPR shows that $^{\bullet}O_2^-$ is the main active species, while the hole has little effect and the $^{\bullet}OH$ radical has no effect (Fig. S15†).

In order to approximate the effect of photocatalysis when applied to the purification of an actual water treatment project, in addition to static tests, continuous flow experiments for BOC/BOI-2 photocatalytic degradation were performed. Phenol, which is more difficult to degrade, was employed as a probe to flow through the reaction system at 1 ml $min^{-1}$. After continuous operation for 45 h, the removal rate of phenol remained at about 70% (Fig. S16†), which not only shows that BOC/BOI-2 has efficient photodegradation activity, but once again proves the excellent stability for BOC/BOI-2.

To fully understand the process of BPA oxidative degradation by photogenerated active species in the BOC/BOI-2 system under $\lambda \geq 420$ nm irradiation, the main degradation intermediates identified with UPLC/MS/MS further down the possible degradation path were analyzed. A total of 10 intermediate products were inferred during BOC/BOI-2 photodegradation BPA. The molecular structure and MS/MS fragmentation information of the oxidation products are displayed in Fig. S17.† Based on these degradation intermediates, the possible degradation pathway of BPA is proposed in Fig. 5. Because the two-electron donating hydroxyl group increased the electron density of each benzene ring, the C–C bond connecting the two benzene rings in BPA is more vulnerable.[43] The β-cleavage of the isopropyl group between the two phenyl groups occurred, forming phenol ($m/z = 93$), 4-isopropylphenol ($m/z = 133$) and 1-(4-hydroxyphenyl)-2-propanol ($m/z = 151$). Phenol is generally oxidized to hydroquinone ($m/z = 109$) and further oxidized to *p*-benzoquinone ($m/z = 107$) that cannot be detected as it is not easily ionized.[44] Meanwhile the active oxygen component further oxidizes 4-isopropylphenol to 4-hydroxycetophenone ($m/z = 135$). Then, the intermediate products were subsequently attacked, yielding small organic acids such as maleic acid ($m/z = 115$), glycolic acid ($m/z = 75$), acetic acid ($m/z = 59$) and 2-gydroxypropionic acid ($m/z = 89$), which were eventually mineralized.

## Dual regulation and charge transfer bridges extend the photogenerated charge lifetime

Inspired by the better photogenerated charge transfer and remarkable photodegradation achieved *via* the dual regulation and charge transfer bridges at the interface, the carrier lifetime was investigated. First, the lifetime of the photogenerated charge in the excited state was quantified from the time-responsive PL spectrum (Fig. 6a and Table S3†). Compared with BOI and BOC with decay lifetimes of 0.58 ns and 0.68 ns, respectively, the decay lifetime of the BOC/BOI-2 is as long as 2.93 ns. The longer excited states of photogenerated charges

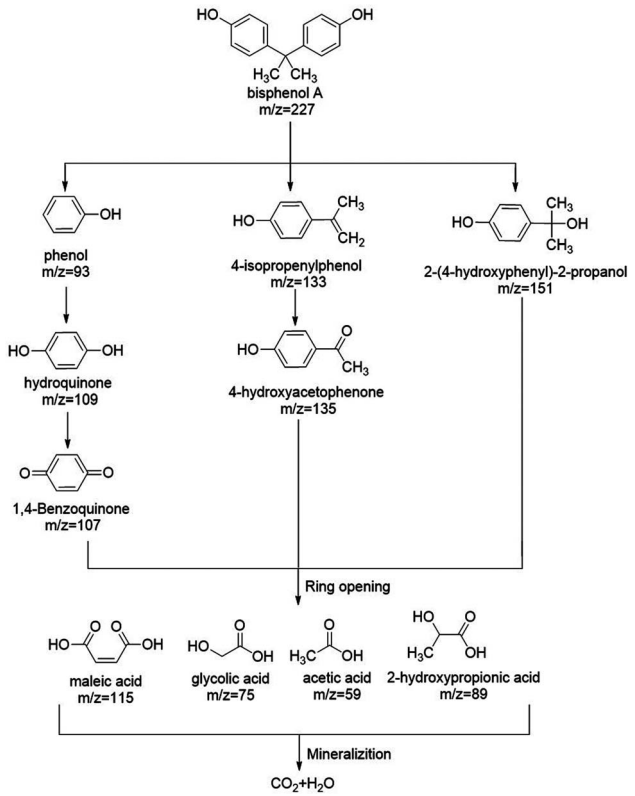


Fig. 5 Proposed degradation pathways of BPA during BOC/BOI-2 photodegradation under $\lambda \geq 420$ nm irradiation.

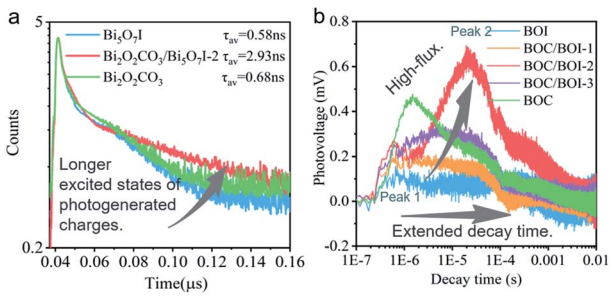


Fig. 6 (a) Time-resolved fluorescence spectrum; (b) lifetime of photogenerated holes detected by time-resolved SPV of the as-prepared samples.

means that they are more likely to migrate to the surface to participate in photocatalytic reactions. Therefore, the lifetime of the photogenerated holes at the photocatalyst surface was tested next. The time-resolved SPV shows that SPV of BOC/BOI-2 is higher than that of other samples (Fig. S18†), which agrees with the SPV results. It should be emphasized that peaks 1 and 2 representing the two successive transfer processes of photogenerated charges can be clearly observed for hybrids (Fig. 6b). Peak 1 is attributed to the photogenerated holes generated by BOI reaching its surface, and peak 2 is the photogenerated holes that migrate to the BOC through the bridge under the action of the dual drivers at the interface. BOC/BOI-2 has the longest decay time (see Table S4† for detailed analysis), meaning that the photogenerated holes reaching the surface have a longer survival time.[45–47] The above charge lifetime proves that, on the one hand, the dual regulation at the BOC/BOI-2 interface enables the photogenerated charge to be separated quickly and efficiently, thereby having a longer carrier lifetime. On the other hand, the extensive charge channels built on the large contact area give high-flux photogenerated charges access to the surface of the photocatalyst, thereby obtaining excellent photodegradation activity (Fig. S19†).

## Conclusions

Through the interfacial band offset and the IEF, dual regulation of the thermodynamic and dynamic conditions of the heterojunction is achieved, promoting the high-speed directional migration of photogenerated charges. In addition, the BOC/BOI heterojunction photocatalyst was constructed with Bi–O chemical bonds as the interface charge transfer bridge for high-flux charge migration. The visible photocatalytic activity of the BOC/BOI heterojunction increased more than 23 times. This strategy is applicable to the interface structure for the high performance of photocatalysts.

## Conflicts of interest

There are no conflicts to declare.

## Acknowledgements

This work was partly supported by the National Natural Science Foundation of China (No. 51978098, 21872077, 21673126, 21761142017, 21621003) and the Collaborative Innovation Center for Regional Environmental Quality.

## Notes and references

1 X. C. M. Zhu, M. Fujitsuka, J. Zhang and T. Majima, *Angew. Chem., Int. Ed.*, 2017, **56**, 5.
2 R. Li, F. Zhang, D. Wang, J. Yang, M. Li, J. Zhu, X. Zhou, H. Han and C. Li, *Nat. Commun.*, 2013, **4**, 1432.
3 X. Chen, Y. Xu, X. Ma and Y. Zhu, *Natl. Sci. Rev.*, 2019, nwz198.
4 X. Chen, S. Shen, L. Guo and S. S. Mao, *Chem. Rev.*, 2010, **110**, 6503–6570.
5 J. Low, J. Yu, M. Jaroniec, S. Wageh and A. A. Al-Ghamdi, *Adv. Mater.*, 2017, **29**, 1601694.
6 Q. Wang, X. Wang, Z. Yu, X. Jiang, J. Chen, L. Tao, M. Wang and Y. Shen, *Nano Energy*, 2019, **60**, 827–835.
7 H. Li, H. Yu, X. Quan, S. Chen and H. Zhao, *Adv. Funct. Mater.*, 2015, **25**, 3074–3080.
8 Y.-Y. Zhang, L. Lang, H.-J. Gu, S. Chen, Z.-P. Liu, H. Xiang and X.-G. Gong, *Phys. Rev. B*, 2017, **95**, 155308.
9 T. L. Kim, M. J. Choi, T. H. Lee, W. Sohn and H. W. Jang, *Nano Lett.*, 2019, **19**, 5897–5903.
10 J. Hou, Y. Wu, S. Cao, F. Liang, Z. Lin, Z. Gao and L. Sun, *Adv. Energy Mater.*, 2017, **7**, 1700171.

 

11 C. Liang, C. G. Niu, L. Zhang, X. J. Wen, S. F. Yang, H. Guo and G. M. Zeng, *J. Hazard. Mater.*, 2019, **361**, 245–258.
12 J. Ran, W. Guo, H. Wang, B. Zhu, J. Yu and S. Z. Qiao, *Adv. Mater.*, 2018, **30**, e1800128.
13 Y. Huang, Z. Guo, H. Liu, S. Zhang, P. Wang, J. Lu and Y. Tong, *Adv. Funct. Mater.*, 2019, **29**, 1903490.
14 J. Li, G. Zhan, Y. Yu and L. Zhang, *Nat. Commun.*, 2016, **7**, 11480.
15 J. Hou, Y. Sun, Y. Wu, S. Cao and L. Sun, *Adv. Funct. Mater.*, 2018, **28**, 1704447.
16 H. Cai, B. Wang, L. Xiong, J. Bi, L. Yuan, G. Yang and S. Yang, *Appl. Catal., B*, 2019, **256**, 117853.
17 J. Li, X. Wu, Z. Wan, H. Chen and G. Zhang, *Appl. Catal., B*, 2019, **243**, 667–677.
18 D. Liu, J. Zhang, C. Li, X. Zhang, X. Chen, F. Wang, M. Shi, R. Li and C. Li, *Appl. Catal. B*, 2019, **248**, 459–465.
19 J. Hou, S. Cao, Y. Sun, Y. Wu, F. Liang, Z. Lin and L. Sun, *Adv. Energy Mater.*, 2018, **8**, 1701114.
20 Y. Guo, W. Shi, Y. Zhu, Y. Xu and F. Cui, *Appl. Catal., B*, 2020, **262**, 118262.
21 K. Steiner, W. Chen and A. Pasquarello, *Phys. Rev. B: Condens. Matter Mater. Phys.*, 2014, **89**, 205309.
22 T. C. Kaspar, P. V. Sushko, S. R. Spurgeon, M. E. Bowden, D. J. Keavney, R. B. Comes, S. Saremi, L. Martin and S. A. Chambers, *Adv. Mater. Interfaces*, 2018, **6**, 1801428.
23 R. Chen, F. Fan, T. Dittrich and C. Li, *Chem. Soc. Rev.*, 2018, **47**, 8238–8262.
24 J. Ran, G. Gao, F. T. Li, T. Y. Ma, A. Du and S. Z. Qiao, *Nat. Commun.*, 2017, **8**, 13907.
25 G. Singh-Bhalla, C. Bell, J. Ravichandran, W. Siemons, Y. Hikita, S. Salahuddin, A. F. Hebard, H. Y. Hwang and R. Ramesh, *Nat. Phys.*, 2010, **7**, 80–86.
26 H. Yao, Y. Cui, D. Qian, C. S. Ponseca Jr, A. Honarfar, Y. Xu, J. Xin, Z. Chen, L. Hong, B. Gao, R. Yu, Y. Zu, W. Ma, P. Chabera, T. Pullerits, A. Yartsev, F. Gao and J. Hou, *J. Am. Chem. Soc.*, 2019, **141**, 7743–7750.
27 M. Zhu, S. Kim, L. Mao, M. Fujitsuka, J. Zhang, X. Wang and T. Majima, *J. Am. Chem. Soc.*, 2017, **139**, 13234–13242.
28 Z. Wang, Y. Huang, L. Chen, M. Chen, J. Cao, W. Ho and S. C. Lee, *J. Mater. Chem. A*, 2018, **6**, 972–981.
29 J. Ran, B. Zhu and S. Z. Qiao, *Angew. Chem., Int. Ed. Engl.*, 2017, **56**, 10373–10377.
30 J. Ran, H. Zhang, J. Qu, B. Xia, X. Zhang, S. Chen, L. Song, L. Jing, R. Zheng and S. Z. Qiao, *Chemistry*, 2019, **25**, 9.
31 S. C. Warren, K. Voitchovsky, H. Dotan, C. M. Leroy, M. Cornuz, F. Stellacci, C. Hebert, A. Rothschild and M. Gratzel, *Nat. Mater.*, 2013, **12**, 842–849.
32 I. Salzmann, G. Heimel, M. Oehzelt, S. Winkler and N. Koch, *Acc. Chem. Res.*, 2016, **49**, 370–378.
33 J. Xu, Y. Teng and F. Teng, *Sci. Rep.*, 2016, **6**, 32457.
34 D. Barreca, F. Morazzoni, G. Andrea Rizzi, R. Scotti and E. Tondello, *Phys. Chem. Chem. Phys.*, 2001, **3**, 1743–1749.
35 J. Hou, S. Cao, Y. Wu, F. Liang, Y. Sun, Z. Lin and L. Sun, *Nano Energy*, 2017, **32**, 359–366.
36 P. W. Anderson, *Phys. Rev.*, 1958, **109**, 1492–1505.
37 G. Feher and E. A. Gere, *Phys. Rev.*, 1959, **114**, 1245–1256.
38 Y. Huang, D. Zhu, Q. Zhang, Y. Zhang, J.-j. Cao, Z. Shen, W. Ho and S. C. Lee, *Appl. Catal., B*, 2018, **234**, 70–78.
39 Z. Zhao, Y. Zhou, F. Wang, K. Zhang, S. Yu and K. Cao, *ACS Appl. Mater. Interfaces*, 2015, **7**, 730–737.
40 X. Feng, W. Zhang, H. Deng, Z. Ni, F. Dong and Y. Zhang, *J. Hazard. Mater.*, 2017, **322**, 223–232.
41 J. Kim, D. Monllor-Satoca and W. Choi, *Energy Environ. Sci.*, 2012, **5**, 7647.
42 Z. Jiang, H. Sun, T. Wang, B. Wang, W. Wei, H. Li, S. Yuan, T. An, H. Zhao, J. Yu and P. K. Wong, *Energy Environ. Sci.*, 2018, **11**, 2382–2389.
43 S. Wang, J. Tian, Q. Wang, F. Xiao, S. Gao, W. Shi and F. Cui, *Appl. Catal., B*, 2019, **256**, 117783.
44 Q. Wang, Z. Liu, D. Liu, G. Liu, M. Yang, F. Cui and W. Wang, *Appl. Catal., B*, 2018, **236**, 222–232.
45 V. Duzhko, V. Y. Timoshenko, F. Koch and T. Dittrich, *Phys. Rev. B: Condens. Matter Mater. Phys.*, 2001, **64**, 075204.
46 S. Li, Q. Zhao, D. Meng, D. Wang and T. Xie, *J. Mater. Chem. A*, 2016, **4**, 16661–16669.
47 Q. Bu, S. Li, K. Zhang, Y. Lin, D. Wang, X. Zou and T. Xie, *ACS Sustainable Chem. Eng.*, 2019, **7**, 10971–10978.